Advances in
Bridge Engineering

ORIGINAL INNOVATION

Open Access

CFD modeling of orthogonal wave-current interactions in a rectangular numerical wave basin

Kai Wei[1*] and Kaiyu Hu[1]

*Correspondence:
kaiwei@home.swjtu.edu.cn

[1] State Key Laboratory of Bridge Intelligent and Green Construction, Southwest Jiaotong University, Chengdu 610031, China

Abstract

Sea-crossing bridges are subject to long-term simultaneous wave and current loadings throughout thier life cycle. The wave-current interaction makes the hydrodynamic load calculation difficult and challenging, especially in simulating the noncollinear wave-current interactions between waves and currents due to potential disturbances such as wall reflections within the observational zone. Therefore, in this study, a numerical flume was built based on the Reynolds time-average (RANS) equation and k-ε turbulence model using the computational fluid dynamics (CFD) software Flow-3D to investigate noncollinear wave-current interaction numerical simulation methods. The collinear wave-current interactions were then numerically simulated using the inflow boundary and mass source wave generation method, and the developed numerical flume was validated with experimental results based on a large-scale wave-current flume. Furthermore, a three-dimensional numerical simulation of complex noncollinear wave-current interactions was developed. The developed rectangular numerical basin based on the collinear wave-current flume was validated with theoretical results regarding wavelength variations in a noncollinear wave-current interaction field. Finally, the effective observation zone of orthogonal wave-current interactions was explored. This study is important for advancing bridge hydrodynamic research into noncollinear wave-current interactions.

Keywords: Sea-crossing bridge, Numerical simulation, Orthogonal wave-current interactions, Noncollinear wave-current interactions, Observation zone

1 Introduction

China has a lengthy coastline and numerous islands. As critical carriers for the extension of highways and railway networks to offshore areas and islands, sea-crossing bridges and their construction have entered an unprecedented period of rapid development (Qin and Gao 2017; Zhao et al. 2021). Situated in complex and variable marine environments, sea-crossing bridges are subject not only to the static and dynamic loads that affect conventional land bridges but also to the long-term influences of waves and currents that impact unison (Wei et al. 2020). When wave-current interactions impact the substructure of a bridge, complicated hydrodynamic loads are created (Wei et al. 2024) (Fig. 1), the effects of which significantly differ from those

Fig. 1 Collapse of sea-crossing bridges

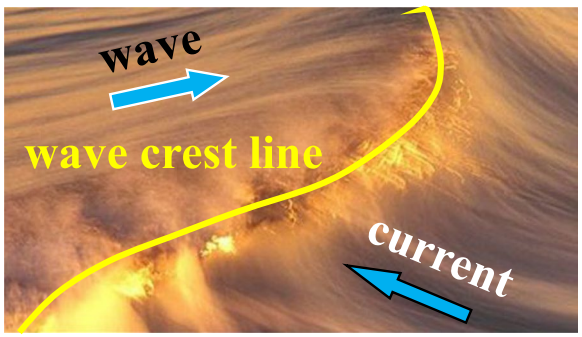

Fig. 2 Noncollinear wave-current interactions

of conventional wave action alone. Numerous studies have demonstrated that waves influenced by currents undergo changes in wave height, wavelength and other characteristics (Zhang et al. 2022; Longuet-Higgins and Stewart 1961), further altering the wave-current field and thereby affecting the structural load. The motion directions of waves and currents often form different angles in marine environments, particularly in straits where a pronounced "venturi effect" is observed (Whitehead 1998). Research indicates that the noncollinear interactions between waves and currents in regions such as the Qiongzhou Strait and Xiamen's Third East Channel are significant (Wei et al. 2023a, b) (Fig. 2), thereby enhancing the complexity of hydrodynamic forces on bridges. This situation introduces considerable risk and technical challenges to bridge construction (Wei et al. 2023a, b; Guo et al. 2022).

Waves and currents are the primary hydrodynamic factors impacting the safety of bridge structures (Zhao et al. 2022). Scholars have conducted extensive research on the interactions between waves and currents. Research into how "wave characteristics change under the influence of current" can be traced back to the 1960s, when Longuet-Higgins (1961) introduced the wave energy flux conservation equation and derived the perturbation solution for the issue of linear waves interacting with codirectional and orthogonal currents, discovering that wave-current interactions can

cause waves to transform into "twists". Based on the findings of Longuet-Higgins, Whitham (1962) deduced the amplitude variations of waves propagating through nonuniform currents. This phenomenon is related to the Doppler frequency shift, with many scholars undertaking related theoretical investigations using the dispersion relation. Peregrine (1976) and Jonsson (1970), based on linear wave and Stokes second-order wave theories, respectively, deduced the changes in wave characteristics under the influence of currents. Brevik (1979; 1980) explored the variations in the amplitude and wavelength of waves under the action of codirectional and contradirectional currents under both rough- and smooth-bed conditions through theoretical derivations and physical flume experiments. Thomas (1981; 1990) conducted flume experiments on the interactions of linear and nonlinear waves with currents of arbitrary vorticity, further validating the effectiveness of Brevik's theoretical and experimental findings.

Experiments and numerical analyses on the interactions of waves and currents have been conducted (Wei et al. 2019); however, most studies have considered only the collinear interactions of waves and currents (Liu et al. 2013). In straits, the direction of the current is relatively fixed, but waves are greatly influenced by strong winds, often resulting in noncollinear occurrences between waves and currents. The oblique interactions of waves and currents can transform long crest waves into short crest waves or even generate extreme waves, posing serious threats to engineering safety (Kang et al. 2020). Marine structures often employ cylindrical sections, with the most adverse loads occurring during collinear interactions between waves and currents. However, the section shapes of piers vary, making hydrodynamic loads highly sensitive to the directions and angles between waves and currents (Wang et al. 2019), rendering the sole consideration of collinear wave-current interactions insufficient for effective structural design. In response to noncollinear wave-current interactions, Lim and Madsen (2016) conducted experiments on wave-current interactions at angles of 60°, 90° and 120° by measuring the velocity distributions and analyzing the field changes induced by wave-current interactions. Jiang and Tai (1993) proposed a coupled refraction-diffraction model for the propagation of random waves in a gentle nonuniform current field and analyzed the characteristics of the wave field at different current velocities during noncollinear wave-current interactions. Johnson (1947) argued that when a wave encounters a current moving at a certain angle, the wavelength, steepness and direction of propagation can all change; therefore, a mathematical model for wave element variations at different wave-current angles was introduced. Li (1984) derived a more comprehensive formula for wave element changes and explored the variations in elements after waves pass through currents at different angles based on Johnson's work. In recent years, with the development of computer technology, computational fluid dynamics (CFD) has also been applied in various studies (Wei et al. 2022; Chen et al. 2021) to effectively simulate the interactions between waves and currents. However, how to better simulate wave-current interactions using CFD, ensuring that the wave-current field is unaffected by extraneous factors such as wall reflections, remains a topic of inquiry. Xiao (2013) simulated wave-current interactions by setting the current inlet and outlet in a flume with a wavemaker boundary. Lin and Liu (1999) proposed a mass source wave generation method, offering a new approach for numerically simulating wave-current interactions. As shown in

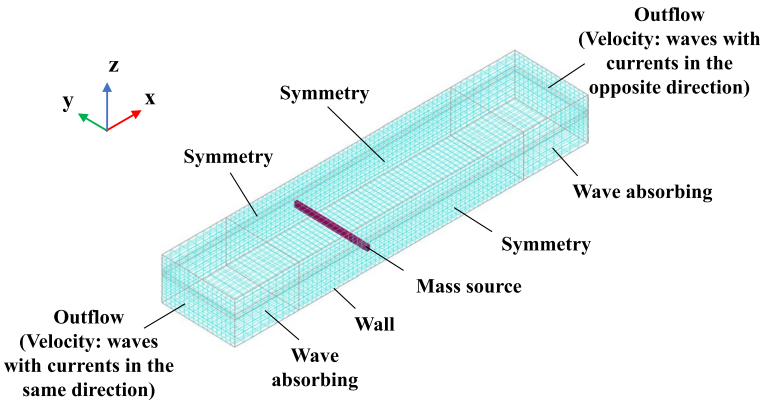

Fig. 3 Wave-current interaction numerical flume model (Ding et al. 2015)

Fig. 3, Ding (2015) used the Sommerfeld boundary to effectively simulate the interactions between waves and currents based on Lin's methodology. While most related studies have concentrated on collinear wave-current interactions, only a few have explored noncollinear wave-current interactions using CFD. However, developing a numerical model for stably simulating the noncollinear interactions between waves and currents remains challenging.

In this study, a numerical flume was built based on the Renolds time-average (RANS) equation and k-ε turbulence model using the computational fluid dynamics software Flow-3D to investigate noncollinear wave-current interaction numerical simulation methods. The collinear wave-current interactions were then numerically simulated using the inflow boundary and mass source wave generation method, and the developed numerical flume was validated using experimental results based on a large-scale wave-current flume. Furthermore, a three-dimensional numerical simulation of complex noncollinear wave-current interactions was developed. The developed rectangular numerical basin based on the collinear wave-current flume was validated with theoretical results from previous research regarding wavelength variations in noncollinear wave-current interaction fields (Li 1984; Li et al. 2004). Finally, the effective observation zone of orthogonal wave-current interactions was explored.

2 CFD modeling of wave-current interactions

2.1 Basic theory

The variance in fluid density is exceedingly marginal and can be deemed an incompressible viscous fluid when waves and currents interact with structures. Given that the fluid density is constant, the equation for the conservation of mass for the fluid can be represented as follows:

$$\nabla \cdot \vec{u} = 0 \tag{1}$$

The fluid adheres to the fundamental control equations of fluid motion, namely, the Navier–Stokes equations (abbreviated as N–S equations). Flow-3D employs the FAVOR (fractional area/volume obstacle representation) mesh handling technique, with its continuity equation and momentum conservation equation presented as follows.

The continuity equation:

$$\frac{\partial}{\partial x}(uA_x) + \frac{\partial}{\partial y}(vA_y) + \frac{\partial}{\partial z}(wA_z) = 0 \tag{2}$$

The momentum equation:

$$\begin{aligned}
&\frac{\partial u}{\partial t} + \frac{1}{V_F}\left(uA_x\frac{\partial u}{\partial x} + vA_y\frac{\partial u}{\partial y} + wA_z\frac{\partial u}{\partial z}\right) = -\frac{1}{\rho}\frac{\partial p}{\partial x} + f_x + g_x \\
&\frac{\partial v}{\partial t} + \frac{1}{V_F}\left(uA_x\frac{\partial v}{\partial x} + vA_y\frac{\partial v}{\partial y} + wA_z\frac{\partial v}{\partial z}\right) = -\frac{1}{\rho}\frac{\partial p}{\partial y} + f_y + g_y \\
&\frac{\partial w}{\partial t} + \frac{1}{V_F}\left(uA_x\frac{\partial w}{\partial x} + vA_y\frac{\partial w}{\partial y} + wA_z\frac{\partial w}{\partial z}\right) = -\frac{1}{\rho}\frac{\partial p}{\partial z} + f_z + g_z
\end{aligned} \tag{3}$$

where u, v and w represent the velocity components of the fluid in the x, y and z directions, respectively; A_x, A_y and A_z represent the area fractions of the fluid in the x, y and z directions, respectively; V_F represents the volume fraction of the fluid; p represents the fluid dynamic pressure; ρ represents the fluid density; f_x, f_y and f_z represent the viscous force accelerations in the x, y and z directions, respectively; and g_x, g_y and g_z represent the gravitational accelerations in the x, y and z directions, respectively, which can be expressed as follows:

$$\begin{aligned}
\rho V_F f_x &= -\left\{\frac{\partial}{\partial x}(A_x\tau_{xx}) + \frac{\partial}{\partial y}(A_y\tau_{xy}) + \frac{\partial}{\partial z}(A_z\tau_{xz})\right\} \\
\rho V_F f_y &= -\left\{\frac{\partial}{\partial x}(A_x\tau_{xy}) + \frac{\partial}{\partial y}(A_y\tau_{yy}) + \frac{\partial}{\partial z}(A_z\tau_{yz})\right\} \\
\rho V_F f_z &= -\left\{\frac{\partial}{\partial x}(A_x\tau_{xz}) + \frac{\partial}{\partial y}(A_y\tau_{yz}) + \frac{\partial}{\partial z}(A_z\tau_{zz})\right\}
\end{aligned} \tag{4}$$

where τ_{ij} represents the shear stress of the fluid, i represents the plane of action, and j represents the direction of action. The equations for τ_{ij} are as follows:

$$\begin{aligned}
\tau_{xx} &= -2\mu\left[\frac{\partial u}{\partial x} - \frac{1}{3}\left(\frac{\partial u}{\partial x} + \frac{\partial v}{\partial y} + \frac{\partial w}{\partial z}\right)\right] \\
\tau_{yy} &= -2\mu\left[\frac{\partial v}{\partial y} - \frac{1}{3}\left(\frac{\partial u}{\partial x} + \frac{\partial v}{\partial y} + \frac{\partial w}{\partial z}\right)\right] \\
\tau_{zz} &= -2\mu\left[\frac{\partial w}{\partial z} - \frac{1}{3}\left(\frac{\partial u}{\partial x} + \frac{\partial v}{\partial y} + \frac{\partial w}{\partial z}\right)\right] \\
\tau_{xy} &= \tau_{yx} = -\mu\left(\frac{\partial v}{\partial x} + \frac{\partial u}{\partial y}\right) \\
\tau_{xz} &= \tau_{zx} = -\mu\left(\frac{\partial u}{\partial z} + \frac{\partial w}{\partial x}\right) \\
\tau_{yz} &= \tau_{zy} = -\mu\left(\frac{\partial v}{\partial z} + \frac{\partial w}{\partial y}\right)
\end{aligned} \tag{5}$$

where μ represents the dynamic viscosity coefficient of the fluid.

Within Flow-3D, six different turbulence models are available for simulating the viscous effects of fluids. These include the Prandtl Mixing Length Model, One-equation Model, Two-equation Model (Standard k-ε Model), Two-equation k-ω Model, Renormalized Group k-ε Model (RNG Model), and Large Eddy Simulation (LES) Model.

The choice of turbulence model directly affects the kinematic viscosity, thereby influencing the computed local shear stress.

The RNG k-ε turbulence model, recognized for its enhanced computational applicability, is selected to close the aforementioned governing equations (Yakhot and Orszag 1986), facilitating the resolution of the turbulent viscosity μ_t. The k and ε equations of the k-ε turbulence model are defined as follows.

$$\frac{\partial k}{\partial t} + \langle u_j \rangle \frac{\partial k}{\partial x_j} = \mu_t \left(\frac{\partial \langle u_i \rangle}{\partial x_j} + \frac{\partial \langle u_j \rangle}{\partial x_i} \right) \frac{\partial \langle u_i \rangle}{\partial x_j} + \frac{\partial}{\partial x_j} \left[\nu_k (\mu + \mu_t) \frac{\partial k}{\partial x_j} \right] - \varepsilon \tag{6}$$

$$\frac{\partial \varepsilon}{\partial t} + \langle u_j \rangle \frac{\partial \varepsilon}{\partial x_j} = \frac{\partial}{\partial x_j} \left[\nu_\varepsilon (\mu + \mu_t) \frac{\partial \varepsilon}{\partial x_j} \right] + C_{\varepsilon 1} \frac{\varepsilon}{k} \mu_t \left(\frac{\partial \langle u_i \rangle}{\partial x_j} + \frac{\partial \langle u_j \rangle}{\partial x_i} \right) \frac{\partial \langle u_i \rangle}{\partial x_j} - C_{\varepsilon 2} \frac{\varepsilon^2}{k} \tag{7}$$

$$\mu_t = C_\mu \frac{k^2}{\varepsilon} \tag{8}$$

where ε represents the rate of dissipation of turbulent kinetic energy and μ represents the dynamic viscosity of the fluid. In this study, the parameters C_μ, ν_k, ν_ε, $C_{\varepsilon 1}$, and $C_{\varepsilon 2}$ are assigned values of 0.085, 1.39, 1.39, 1.42, and 1.92, respectively.

2.2 Numerical setup of the wave-current interaction flume

A numerical flume was built using Flow-3D numerical software (Fig. 4). The flume was 68 m long, 1.8 m wide, and 1.0 m high. To mitigate adverse impacts arising from simultaneous wave and current generation at the boundary in anticipation of wave-current interactions, a mass source wave generation method and an inflow boundary were employed. The mass source, positioned at x = 0 m, was configured as a rectangular prism with dimensions of $L_m \times H_m \times W_m$. The detailed dimensions and positioning were adapted following the methodology described by Lin and Liu (1999). In the model, $L_m = 0.024$ m, $H_m = 0.12$ m, and $W_m = 1.8$ m. The mass source generates waves toward both ends, so the wave absorption must be set to a length of 2 times the wavelength at both ends of the flume (the function is equivalent to the wave absorption of the

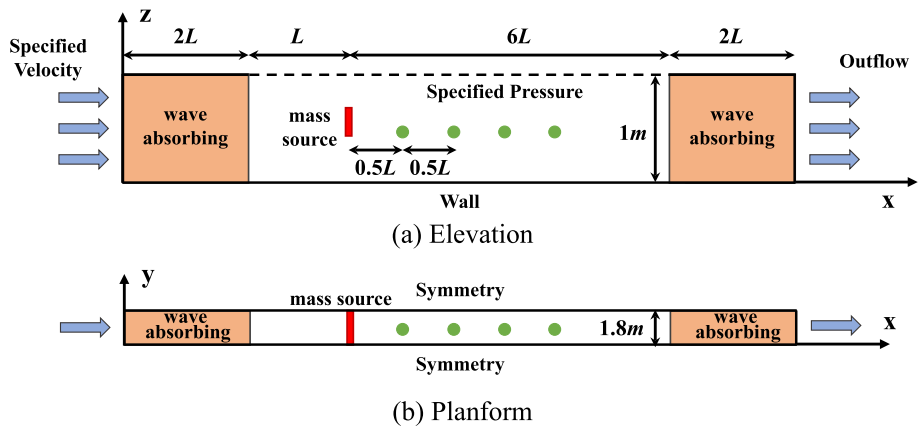

Fig. 4 Numerical flume

experiment). The following boundary conditions were implemented: a wall boundary at the bottom, a symmetric boundary on the sides, and a specified pressure boundary at the top (the pressure was equal to one standard atmosphere). Under pure wave conditions, both ends were set as outcurrent boundaries. Under wave-current interaction (same direction) conditions, the left boundary was set as the specified velocity boundary, and the right boundary was set as the outflow boundary, wherein the pressure at the outflow boundary varied with the hydrostatic pressure through the water depth. Furthermore, to monitor the temporal and spatial variations in the wave surface, wave monitoring points were strategically placed 1, 1.5, and 2 wavelengths away from the mass source within the numerical model (sampling frequency of 100 Hz) to observe the wave surface time series at different locations.

Employing the model delineated above, a stable wave-current interaction field is generated via the following steps:

(1) The current is generated using a specified velocity boundary, with the initial field set as a uniform current at the target velocity.
(2) Once the field reaches stability, the wave-current interaction is simulated using the mass source wave generation method. The target wave is a Stokes fifth-order wave, and the volumetric current rate VFR of the mass source is expressed as follows:

$$V_{FR} = \frac{2CW_m}{k} \sum_{n=1}^{5} \lambda_n \cos\left[n\left(k'x - \omega t\right)\right] \tag{9}$$

where C represents the phase velocity of the targeted wave, k represents the wavenumber, λ_n represents the determination coefficient, and ω represents the angular frequency. In addition, coefficient 2 indicates that the mass source concurrently generates two sets of waves with opposing propagation directions.

(3) To ensure computational stability during the initial phase, the V_{FR} is multiplied by an incrementing envelope function E, which starts at zero, allowing the wave height to gradually increase to the target value (Ding et al. 2015). The envelope function is expressed as follows.

$$E = \begin{cases} 1 - \exp\left(-\frac{2t}{T}\right) & t/T \le 3 \\ 1 & t/T > 3 \end{cases} \tag{10}$$

where T represents the wave period.

Additionally, to prevent the mass source from influencing the current field during numerical simulation, the mass source is configured as a porous medium with a porosity of 1; thus, the object is fully porous and is nonsolid.

Numerical wave absorption primarily relies on the Sommerfeld radiation boundary condition (applicable to linear waves) and the wave absorption damping method. In this

paper, the wave absorption damping method was employed, and a damping coefficient was assigned to achieve efficient wave absorption. To ensure that the current enters and exits the computational domain steadily when simulating wave-current interactions, the wave absorption setting must account for the background current velocity. The following specific formula is used to address the motion of fluid particles:

$$\frac{\partial u_i}{\partial t} + u_j \frac{\partial u_i}{\partial x_j} = -\frac{1}{\rho} + \frac{\partial^2 \nu u_i}{\partial x_j^2} - c(u_i - U_i) \tag{11}$$

where ν represents the dynamic viscosity, c represents the damping coefficient, and U_i represents the background current velocity. The numerical setting adopted inside the wave absorption can be kept constant, or it can linearly increase with distance in the downstream direction. The mathematical formula is as follows:

$$c = c_0 + d_s \cdot \frac{c_1 - c_0}{L_d} \tag{12}$$

where c_0 and c_1 represent the damping coefficients at the upstream and downstream endpoints of the wave absorption, respectively, d_s represents the distance from the point to the upstream endpoint, and L_d represents the length of the wave absorption.

2.3 Numerical setup of the orthogonal wave-current interaction basin

A three-dimensional wave-current numerical basin is established using the CFD software Flow-3D. Due to the characteristics of orthogonal wave-current interactions, unlike collinear interactions, before simulation is conducted, the possibility of the current influencing the direction of wave propagation is considered, as is the possibility of wave reflection from walls affecting the observation area. Therefore, the length and width of the numerical basin are increased as much as possible to enlarge the wave-current interaction area, facilitating subsequent observation. As shown in Fig. 5, the length of the basin is set to 11 times the wavelength L, the width is set to 4 times the wavelength L, and the height is set to 1.5 h, where h is the water depth. Mass source wave generation is employed at x = 0 m. Wave absorbing blocks with a length of 2 L are set on both sides of the basin to absorb waves

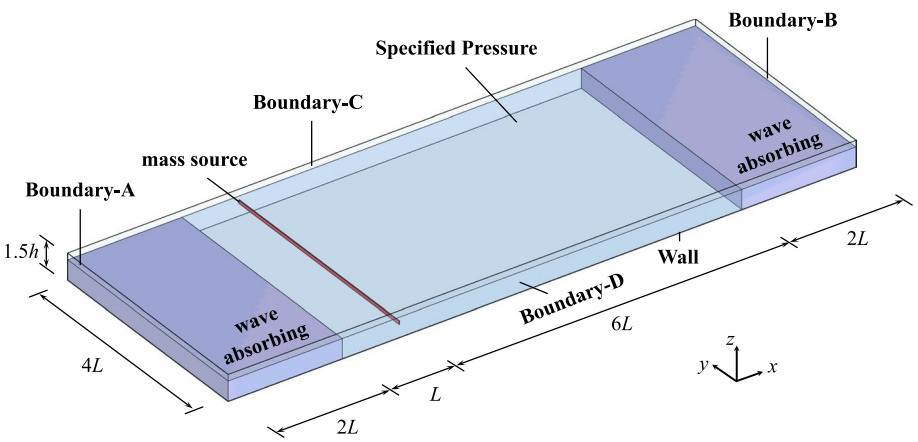

Fig. 5 Numerical basin

Table 1 Boundary settings

	BD-A	BD-B	BD-C	BD-D	Bottom	Top
Pure wave	Outflow	Outflow	Symmetry	Symmetry	Wall	Pressure
Orthogonal	Outflow	Outflow	Outflow	Velocity	Wall	Pressure
Oblique (0°-90°)	Velocity	Outflow	Outflow	Velocity	Wall	Pressure
Oblique (90°-180°)	Outflow	Velocity	Outflow	Velocity	Wall	Pressure

Table 2 Grid size and computational efficiency

Size	△x (m)	△y (m)	△z (m)	Grid number	Time (s)
Thick	0.056 (L/100)	0.084	0.017 (H/15)	21,534,590	21,956
Medium	0.045 (L/125)	0.0675	0.013 (H/20)	40,284,216	44,344
Fine	0.036 (L/155)	0.054	0.010 (H/26)	82,385,808	99,904

propagating toward the sides. Studies have shown that when the distance between a wave absorbing block and a mass source is greater than 0.5 L, the wave absorbing block has a negligible effect on the wave generation effect of the mass source (Chen and Hsiao 2016). In this paper, the minimum distance between the wave absorbing blocks and the mass source is L, which meets the aforementioned requirement.

The boundary conditions of the numerical basin vary depending on the different forms of wave-current interactions, as shown in Table 1. Specifically, when simulating a pure wave, the initial condition is set as static water; when simulating a wave-current interaction, the initial condition is set as a uniform current field with a velocity equal to the target current velocity.

The computational accuracy and efficiency of the numerical software Flow-3D depend on the number and quality of the grid divisions. Using a larger grid size can shorten the computation time while reducing the computational accuracy, especially when capturing the fluid morphology around structures. A smaller grid size, in contrast, can enhance computational accuracy but significantly reduces computational efficiency (Xie et al. 2021). In this paper, to balance the computational accuracy and efficiency, pure wave conditions with H = 0.26 m, T = 1.9 s, and d = 1.93 m are taken as examples, and thick, medium, and fine grids are compared for analysis. The sizes of the three types of grids are shown in Table 2, and their division details are shown in Fig. 6. The "time" in Table 2 represents the time cost of the same scenario under the three grid settings.

For different grid size schemes, the grid convergence index (GCI) method is used to conduct grid independence analysis to determine a more reasonable grid division approach, providing a foundation for subsequent research. The GCI (Wei et al. 2022) is used to evaluate the convergence of numerical simulations under different grid divisions. It is defined as a unified measure of grid refinement (Roache 1997) and can be calculated using the following formula.

$$f_i = f_{exact} + g_p h_i^p + O\left(h_i^{p+1}\right) \tag{13}$$

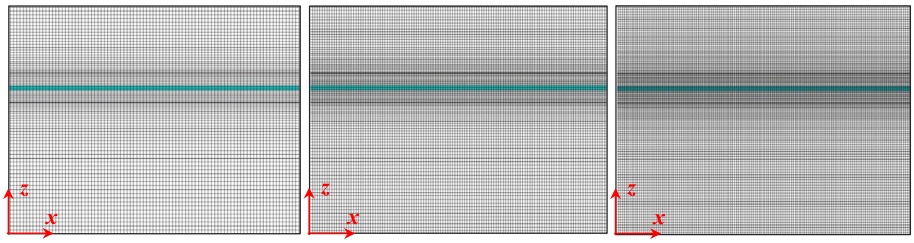

(a) thick (b) medium (c) fine

Fig. 6 Three different precision grids

Table 3 The GCI for the wave height

Target variable	$\varepsilon_{1,2}$	$\varepsilon_{2,3}$	R	p	$GCI_{1,2}$(%)	$GCI_{2,3}$(%)
Wave height H	0.005	0.0023	0.46	4.1088	4.07	0.65

$$r_{i,i+1} = \left(\frac{N_{i+1}}{N_i}\right)^{1/3} \tag{14}$$

$$\delta_{r(i,i+1)} = \left|\frac{f_i - f_{i+1}}{f_{i+1}}\right| = \left|\frac{\varepsilon_{i,i+1}}{f_{i+1}}\right| \tag{15}$$

$$\frac{\delta_{i,i+1}}{r_{i,i+1}^p - 1} = \frac{\delta_{i+1,i+2} r_{i+1,i+2}^p}{r_{i+1,i+2}^p - 1} \tag{16}$$

$$GCI_{i,i+1} = F_s \frac{r_{i,i+1}^p \delta_{r(i,i+1)}}{r_{i,i+1}^p - 1}, GCI_{i+1,i+2} = F_s \frac{\delta_{r(i+1,i+2)}}{r_{i+1,i+2}^p - 1} \tag{17}$$

where f_i represents the numerical discrete solution, f_{exact} represents the exact solution, and g_p represents the coefficient of the pth-order error term, which remains constant regardless of the mesh size. The symbol $\boldsymbol{O}$ represents higher-order infinitesimals, r represents the mesh refinement ratio, N represents the number of mesh elements, p represents the convergence order, and F_s represents the safety factor, which is set as 1.25 when comparing the results under three types of meshes (Roache 1997). $R = \varepsilon_{2,3}/\varepsilon_{1,2}$ represents the convergence rate, and the grid is monotonically convergent when $0 < R < 1$ (Samion et al. 2019).

Table 3 shows the calculated results of the GCI for the three types of meshes. The results show that the GCI values progressively decline from the thick to the medium to the fine mesh, with the value of $GCI_{2,3}$ being merely 0.65%, which is below the 3% threshold, thus satisfying the convergence criteria. After deliberation, the medium mesh is ultimately selected for the subsequent numerical models. In subsequent research on wave-current interactions, the mesh was divided into $\triangle$x, $\triangle$y, and $\triangle$z with L/125, L/85, and H/20, respectively.

3 Numerical feasibility validation

3.1 Experimental validation

The physical wave-current interaction experiments described herein were conducted in a large section of a wave-current flume at the Zhoushan Campus Laboratory of Ocean College, Zhejiang University. This extensive flume measures 75 m in length, 1.8 m in width, and 2.0 m in height, with a maximum experimental water depth of 1.5 m, a maximum current rate of 0.8 m^3/s, a current generation accuracy of ≤ 0.03 m/s, a wave period range of 0.5–5.0 s, and a wave height range of 0.02–0.60 m. The flume's frontend is equipped with a hydraulic servo-driven wave-making system and a current generation system, both of which can work in tandem to generate waves (regular and irregular) and currents simultaneously, thus simulating the interactions of waves and currents within the flume. The flume is primarily divided into sections for wave and current generation, transition, experimental testing, wave absorption, and recirculation. A wave absorbing device made of porous polymer material and an automatic recirculation system is present at the terminus of the flume. These devices are designed to dissipate most waves of varying depths and consume a significant portion of wave energy, transporting water from the bottom of the flume back to the current generation section to cycle. A schematic overview of the large section of the laboratory wave-current flume is shown in Fig. 7.

Stainless steel rails are installed on top of the H-shaped steel supports on both sides of the testing section in the flume; through the mounting of aluminum profiles and the setup of related instruments, the equipment is allowed to slide forward and backward (along the x-axis). Moreover, the flume is equipped with a velocimeter mounting frame, which, through the use of an electric switch, facilitates forward and backward (x-axis), left and right (y-axis), and upward and downward (z-axis) movements of the velocimeter, thus conveniently monitoring the current velocity at targeted points.

During the experiments, the current velocity was measured using an acoustic Doppler velocimeter (ADV). The fixation frame for the velocimeter and the method of securing the velocimeter are illustrated in Fig. 8(a), while the orientation and

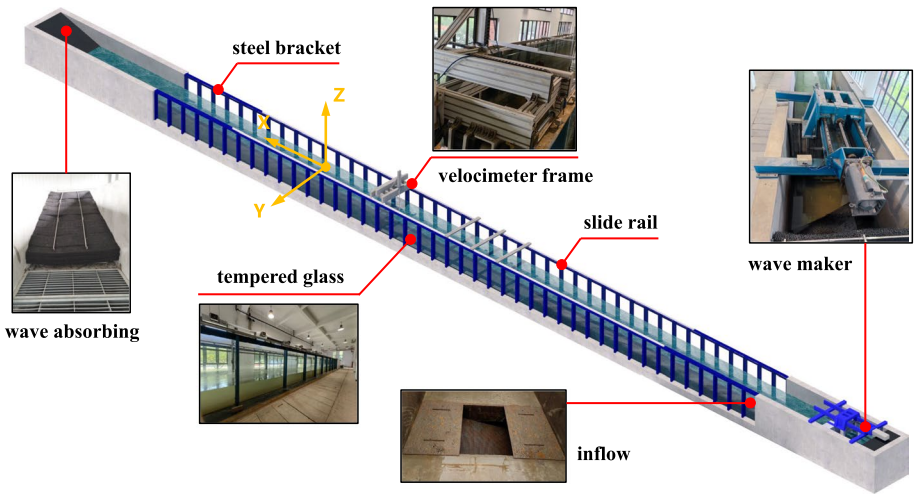

Fig. 7 Experimental flume and equipment

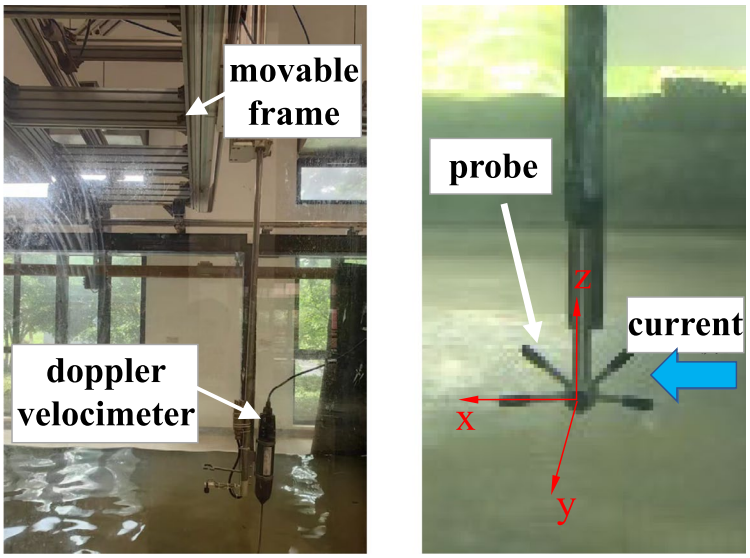

Fig. 8 Acoustic Doppler velocimeter

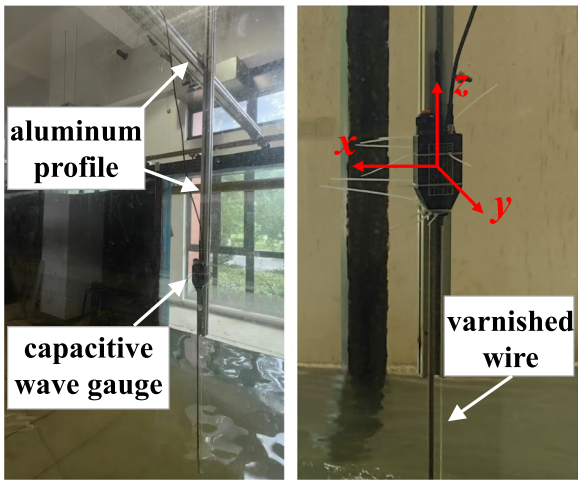

Fig. 9 Wave height gauge and arrangement

construction of the velocimeter probe are displayed in Fig. 8(b). The current velocity must be calibrated before the experiments are conducted. Once the current velocity meets the experimental requirements, subsequent experiments can be conducted. The Doppler velocimeter has a sampling frequency range of 0–200 Hz and a current velocity measurement range of 0–4 m/s, with a precision of 1/1000. The sampling frequency of the velocimeter during the experiments is set to 100 Hz.

In the experiment, a capacitive wave height gauge is utilized to monitor changes in the liquid surface height. The fixing method of the wave height gauge, as depicted in Fig. 9 (left), involves horizontal and vertical fixation via aluminum profiles. A detailed view of the wave height gauge is shown in Fig. 9 (right). Its operating principle

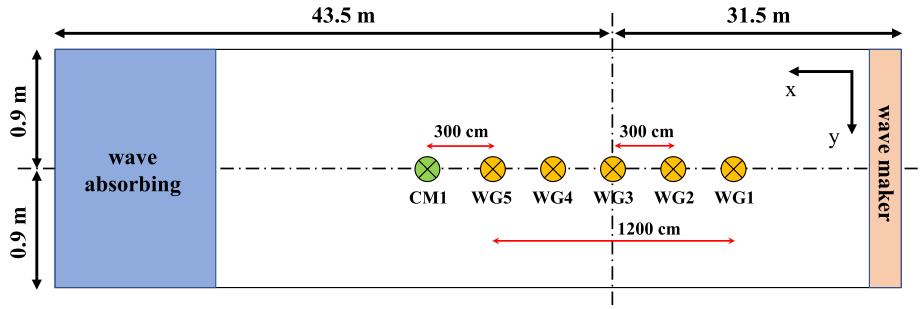

Fig. 10 Instrument layout

Table 4 Scenarios

No	Water depth d (m)	Wave height H (m)	Period T (s)	Current velocity U (m/s)	Target
①	0.6	0.25	2.5	—	Experimental, numerical, theoretical waveform comparison
②		0.20	1.5	—	
③		0.25	2.5	0.05	Experimental and numerical waveform comparison
④				0.10	
⑤				0.15	
⑥				0.20	

involves using enameled wires stretched between the ends of a metal arm to form a capacitor. This design leverages the different dielectric constants of water and air. Changes in capacitance are measured by monitoring the depth to which the enameled wire is submerged to determine the height of the liquid surface. This type of wave height gauge is known for its stability and high precision. The wave height gauge used in this experiment has a range of 0–80 cm, a sampling frequency of 100 Hz, and a measurement precision of 1/500.

In the experimental testing section, instruments, including wave height gauges and velocimeters, are deployed. All the instruments are positioned along the central axis of the flume, 0.9 m away from the sidewalls. To allow waves to fully develop and interact with the current and to prevent reflections from waves not dissipating at the end of the flume, wave height gauges were arranged within the range of 25.5 m-37.5 m from the flume's starting end, as illustrated in Fig. 10. Five wave height gauges are set up in a straight line to monitor changes in the wave form in the direction of propagation, with 3 m between adjacent gauges, sequentially named WG1, WG2, WG3, WG4, and WG5. To accurately calibrate the current velocity in the field, a velocimeter, named CM1, was placed 3 m behind WG5.

Two sets of conditions are utilized for simulating the physical wave field: one with a water depth of 0.6 m, a wave period of 2.5 s, and a wave height of 0.25 m and the other with a water depth of 0.6 m, a wave period of 1.5 s, and a wave height of 0.20 m. To simulate the wave-current field, current velocities of 0.05 m/s, 0.10 m/s, 0.15 m/s, and 0.20 m/s are chosen, and the relevant parameters are presented in Table 4. To increase the accuracy of the experimental test results, wave generation is conducted

after the water current stabilizes, and the data collection period is no less than 30 wave periods. Each set of experimental conditions is used for testing three times, with the experimental results reported as the average values obtained from the stable variation segments of the data.

The experimental and numerical wave surface time histories under two pure wave conditions were compared with the theoretical waveform of the Stokes fifth-order wave, as shown in Fig. 11. The wave-absorbing slope at the end of the experimental flume cannot dissipate all the wave energy; as a result, some reflected waves still impact the experiment. However, the experimental waveforms, numerical waveforms, and theoretical waveforms align well. Compared with that of the theoretical data, the error rates of the experimental and numerical data are less than 5%. Moreover, both the experimental and numerical waveforms remain stable over several periods, demonstrating that both the experimental and numerical flumes possess satisfactory wave-making capabilities and can be used for subsequent related research.

The experimental wave surface time history and numerical wave surface time history under the four wave-current interaction conditions are compared in Fig. 12. With current velocities of 0.05 m/s, 0.10 m/s, 0.15 m/s, and 0.20 m/s, the relative errors between the numerical solutions and experimental solutions are 0.8%, -0.4%, -0.9%, and -4.1%, respectively. The relative errors of the wave-current interaction results under different velocities are all less than 5%, indicating that the software Flow-3D and the modeling method used in this paper can accurately and effectively simulate the wave-current interactions and can be utilized for subsequent related research.

3.2 Theoretical validation

Based on the findings of Johnson (1947), Li (1984; 2004) derived a more comprehensive formula for wave element variations, exploring the changes in wave elements after waves pass through a current area at various angles.

When a wave diagonally enters a current area from a still water area, not only do the wavelength and wave height change but also as the wave speed alters, the direction of wave propagation changes as well, resulting in the refraction phenomenon illustrated in Fig. 13.

The absolute wave speed C_a in the current area can be represented as follows:

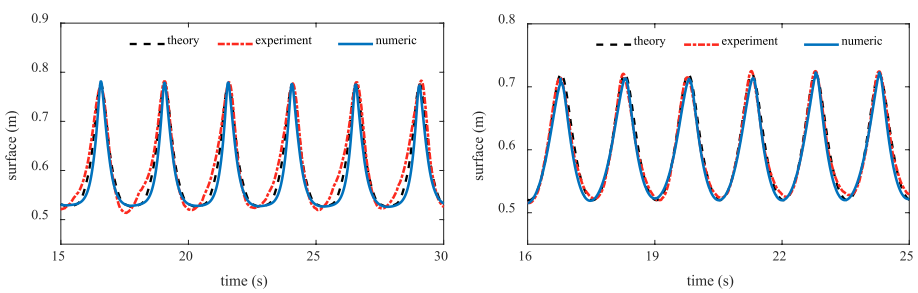

(a) H = 0.25 m, T = 2.5 s, d = 0.6 m (b) H = 0.2 m, T = 1.5 s, d = 0.6 m

Fig. 11 Comparison of theory, numeric and experiment

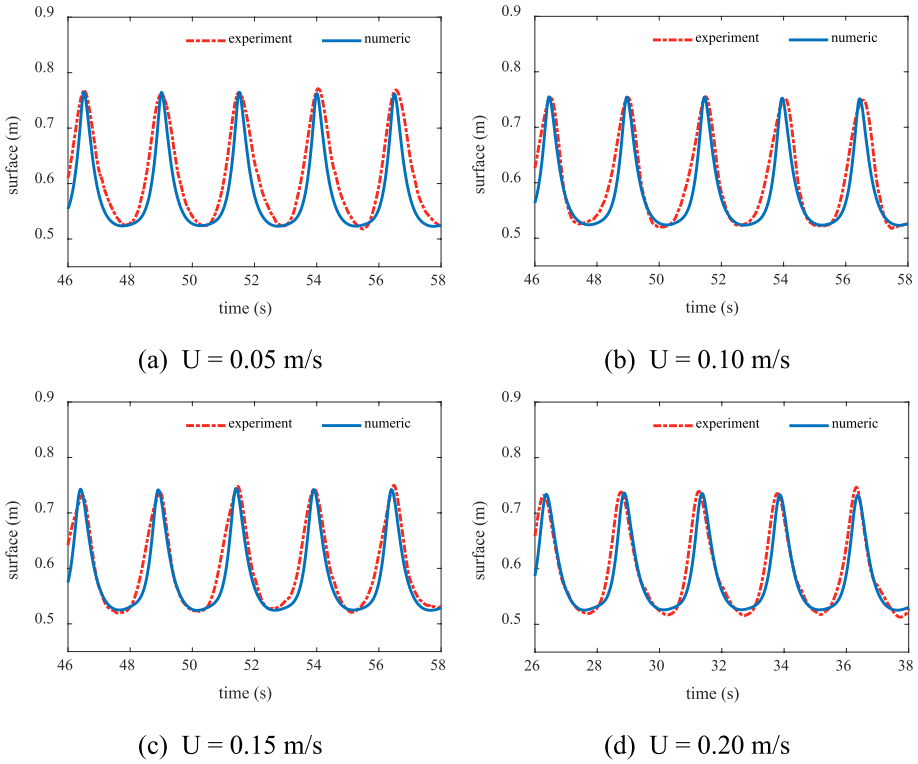

Fig. 12 Wave surface time history under different current velocities

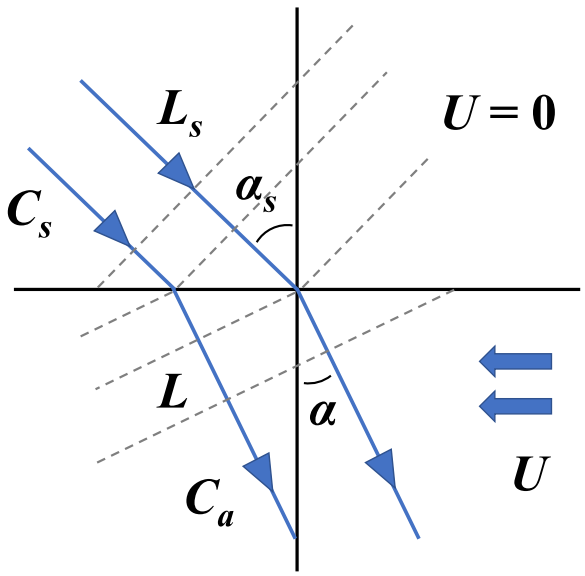

Fig. 13 Wave diagonally interacting with current

$$C_a = C_r + U \sin \alpha \tag{18}$$

where U represents the current velocity, α is the angle of refraction, which also represents the angle between the wave orientation and the normal to the current, and C_r is

the wave velocity relative to the current, which can be determined using the following equation:

$$C_r = \sqrt{\frac{g}{k_r} \tanh k_r d} \tag{19}$$

where d represents the water depth and k_r represents the current wavenumber, which is also represented by k, $k_r = k = 2\pi/L$. L represents the wavelength. Additionally, the value of C_a can also be expressed using the following equation:

$$C_a = \frac{L}{T_a} \tag{20}$$

where T_a represents the actual period of the wave and L represents the wavelength.

In areas without current and those with current, the propagation of waves should remain continuous. Therefore, the wavenumber in the direction of the current should be equal in both areas. Assuming that the wave elements in still water are denoted with the subscript '*s*', then:

$$k_s \sin \alpha_s = k \sin \alpha \tag{21}$$

or

$$\frac{L_s}{\sin \alpha_s} = \frac{L}{\sin \alpha} \tag{22}$$

When the wave is in a steady state, the actual period of the wave in both regions should also remain unchanged, which means the following:

$$T_s = T_a \tag{23}$$

or

$$T = \frac{C_a}{L} = \frac{C_s}{L_s} \tag{24}$$

From the above equations, the formula for calculating the change in wavelength can be derived, which is solved using the iterative method:

$$\frac{L}{L_s} = \left(1 - \frac{U}{C_s} \sin \alpha_s\right)^{-2} \frac{\tanh kd}{\tanh k_s d} \tag{25}$$

A numerical wave basin is employed to conduct noncollinear wave-current interaction simulations at various angles. The wavelength data after the noncollinear wave-current interactions are compared with the theoretical solution for wavelength variation proposed by Li. The results are shown in Table 5 and Fig. 14.

As shown in Table 5, the numerical simulation results closely align with the theoretical wavelength changes. The relative deviations for the noncollinear wave-current interaction outcomes across six different angles do not exceed 4%, indicating that the software can adequately simulate the noncollinear wave-current interactions.

Table 5 Theoretical verification

Angle (°)	d/L_s	U/C_s	Theoretical wavelength (m)	Numerical results (m)	Relative deviation (%)
30	0.344	0.101	6.5933	6.3802	3.23
45			6.3823	6.2695	2.27
60			6.1505	6.0315	1.93
120			5.1357	5.3097	-3.4
135			4.9531	5.0055	-1.06
150			4.8113	4.7698	0.87

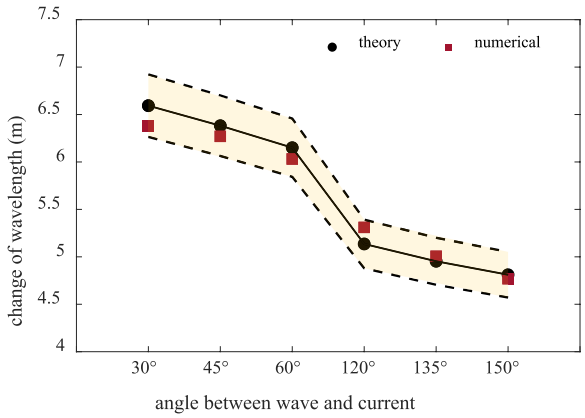

Fig. 14 Comparison of wavelength changes

4 Results and discussion on orthogonal wave-current interactions

4.1 Scenario settings and probe layout

Noncollinear wave-current interactions differ from collinear wave-current interactions. Due to the disturbance effect on the wave-current field by lateral boundaries, stable and reasonable effective observations should be selected when researching the characteristics of the noncollinear wave-current interaction field. This study focuses on the wave-current orthogonal field, wherein the angle between the wave and the current is the largest and most notable. The effective observation zone discovered through this interaction field scenario can be used to observe other angle wave-current fields. Different wave heights and current velocities are utilized to simulate wave-current orthogonality to determine the effective observation zone of the field. The specific data are provided in Table 6.

Because wave reflections near the boundaries of a numerical wave basin can adversely affect wave-current field observations, the regions within one wavelength from the upper boundary and half a wavelength from the lower boundary in the width direction of the basin are initially excluded. The probes are arranged within the range illustrated in Fig. 15, and their arrangement is depicted in Fig. 16. The range where probes are placed does not represent the final observation area. The data from these probes must be analyzed to select a reasonable observation zone for the wave-current orthogonal field.

Table 6 Scenarios

No	Content	Water depth d (m)	Wave elements		Current velocity U (m/s)	Angle α (°)
			Wave depth H (m)	Period T (s)		
①	Orthogonal wave-current interactions	1.93	0.26	1.9	0.2	90
②			0.26	1.9	0.3	90
③			0.26	1.9	0.6	90
④			0.285	1.9	0.3	90
⑤			0.32	1.9	0.3	90

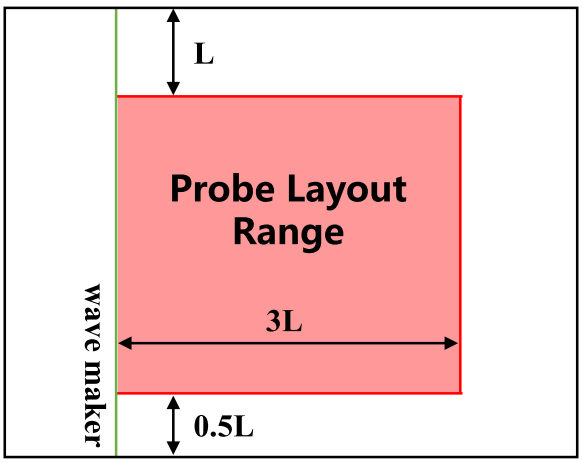

Fig. 15 Probe layout range

4.2 Characteristics of an orthogonal wave-current interaction field

By observing the wave surface time history of probes, the stability of the wavefront changes is assessed to determine whether the corresponding zone can be used for subsequent research. To select a reasonable observation zone more scientifically, wave surface time histories are taken from a stable period at each probe, and the wave peak and trough values within no less than four periods are extracted to perform a standard deviation analysis. The stability of the wave-current field in the corresponding zone can be determined by evaluating the magnitude of the standard deviation.

Figure 17 shows the wave surface time histories at six different orientation probes with good stability for case 2 in Table 6. The wave surface time histories exhibit regular and stable changes, indicating that the effective observation zone can be selected within the range of the probe arrangement shown in Fig. 15. During the orthogonal wave-current simulation, the time for the current field to stabilize is 30 s, and the observation time range can be chosen from 5 to 25 s (the start of wave generation is set at 0 s).

4.3 Determination of the orthogonal wave-current interaction zone

A significant variation in the wave surface time history at a probe indicates that the location is not suitable for subsequent observation. Therefore, the standard deviation

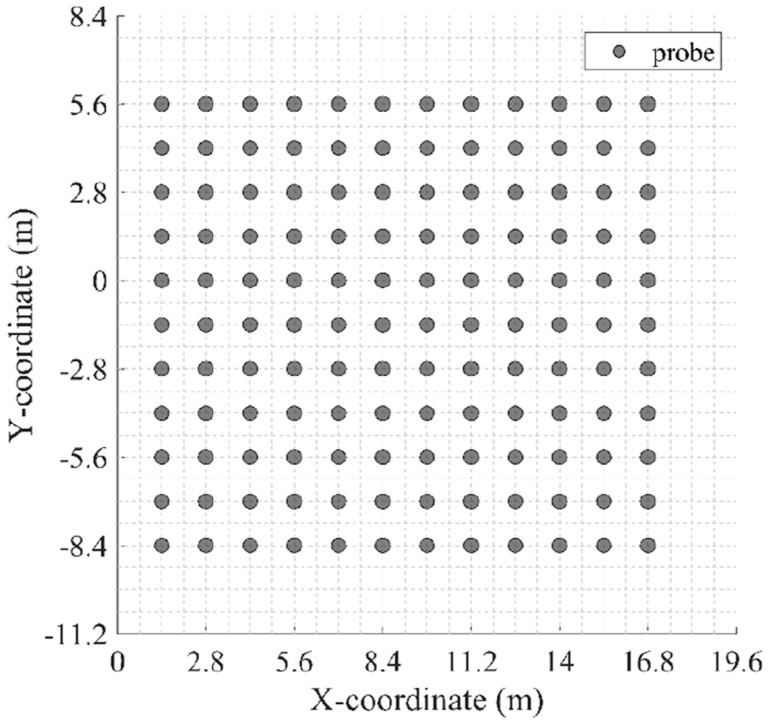

Fig. 16 Sketch of probes layout

of the wave surface over a stable period must be calculated for each probe within the arranged zone. Figure 18 shows a standard deviation contour map of the surface stability under different wave heights and current velocities. The standard deviation reflects the degree of dispersion of the wave height data monitored at each probe, and is the square root of the arithmetic mean of the square deviation between the standard value of each wave height and the mean value of the wave height. A larger standard deviation indicates weaker stability in the corresponding zone; conversely, a smaller standard deviation indicates better stability. Zones with excessively large deviations must be excluded.

The zone selection method described above can eliminate areas with significant wave height changes, but it cannot cope with some special situations, as shown in Fig. 19. Due to the possibility of the surface exhibiting phenomena such as continuous rising or falling with small wave height changes (Fig. 19(a) or unstable fluctuations (Fig. 19(b), a second zone selection method is proposed. This method is used to calculate the standard deviation of the difference between the peak/trough values and the still water level over a certain period.

Figure 20 is a standard deviation contour map obtained via the second method of wave surface stability analysis under different wave heights and current velocities. Similarly, a larger standard deviation indicates weaker stability in the corresponding zone, while a smaller standard deviation indicates better stability. Zones with excessively large deviations must be excluded.

Overlaying the zones analyzed for stability, as described above, illustrates that the unstable regions are primarily concentrated near the upper and lower boundaries of

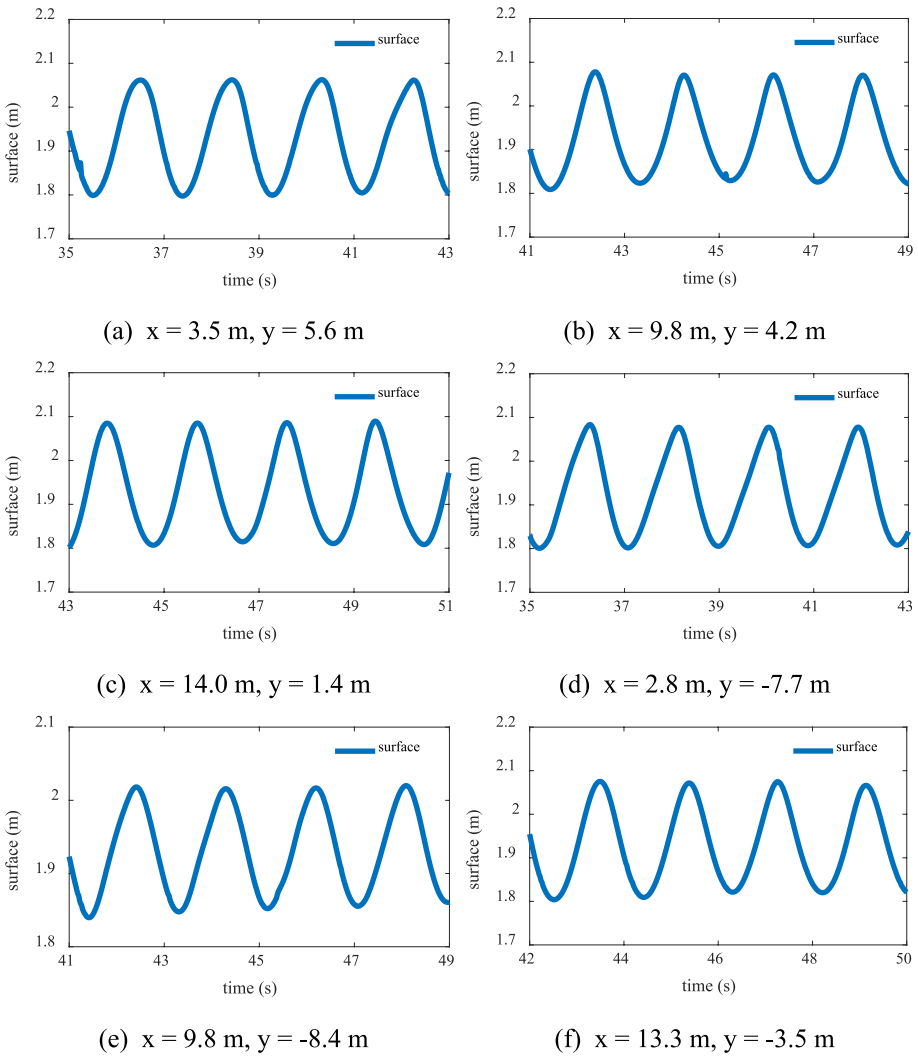

Fig. 17 Wave surface time history at some probes

the numerical basin and at locations far from the wave mass source. The areas near the upper and lower boundaries are not selected primarily because of factors such as wave reflection; the areas far from the wave mass source are not selected because of factors such as wave energy dissipation. The areas with better stability are chosen as the effective observation zone for the orthogonal wave-current interaction field, as shown in Fig. 21. Taking the model in the paper as an example, the effective observation zone can be chosen within a range of 2×2 L.

5 Conclusions

In this paper, a numerical flume model of collinear wave-current interactions was validated via experimental results based on a large-scale wave-current flume. A three-dimensional numerical simulation of complex noncollinear wave-current interactions was developed. The developed rectangular numerical basin was validated with theoretical results regarding wavelength variations in a noncollinear wave-current

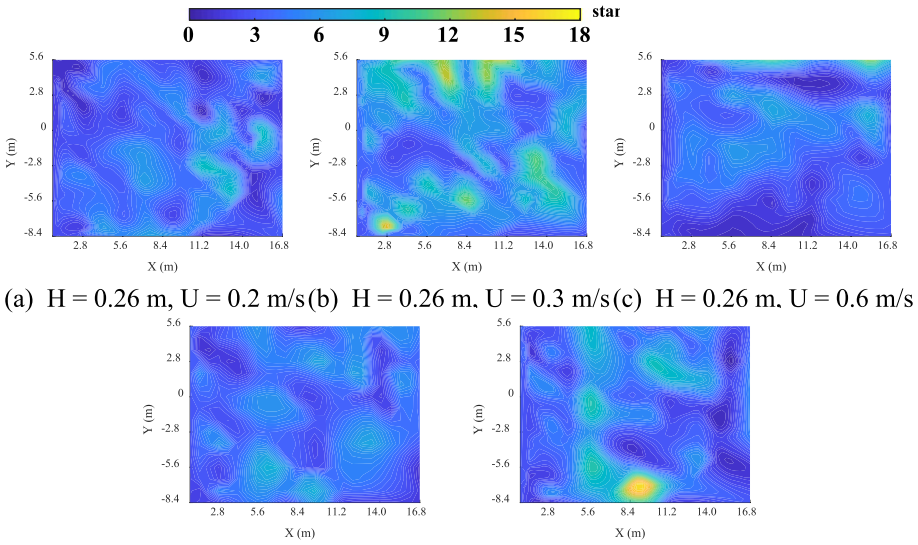

Fig. 18 The first method of zone selection

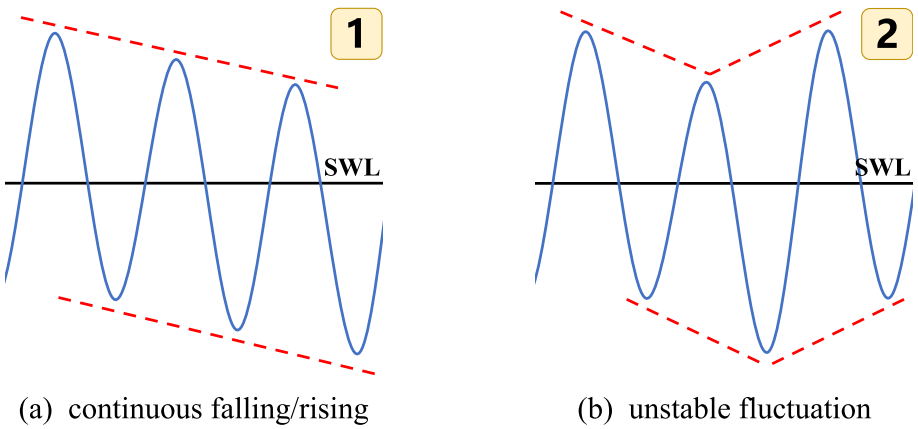

Fig. 19 Situations of instability not identified by the first method

interaction field. The effective observation zone of orthogonal wave-current interactions was explored. The main conclusions are as follows:

(1) Large-scale wave-current flume experiments were conducted under various current velocities to test the codirectional interactions between waves and currents. The experiments were replicated using CFD software, validating the accuracy and feasibility of simulating collinear wave-current interactions in a numerical flume.
(2) A numerical basin was built to investigate numerical simulation methods for noncollinear wave-current interactions. Noncollinear wave-current interactions were simulated at angles of 30°, 45°, 60°, 120°, 135°, and 150°. The results were compared with those of previous theoretical derivations regarding the wavelength changes in

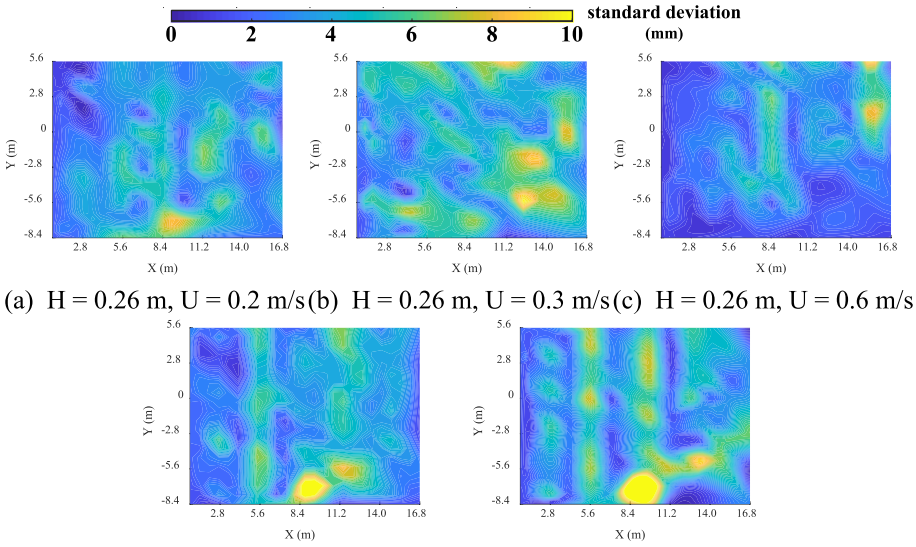

(a) H = 0.26 m, U = 0.2 m/s (b) H = 0.26 m, U = 0.3 m/s (c) H = 0.26 m, U = 0.6 m/s

(d) H = 0.285 m, U = 0.3 m/s (e) H = 0.32 m, U = 0.3 m/s

Fig. 20 The second method of zone selection

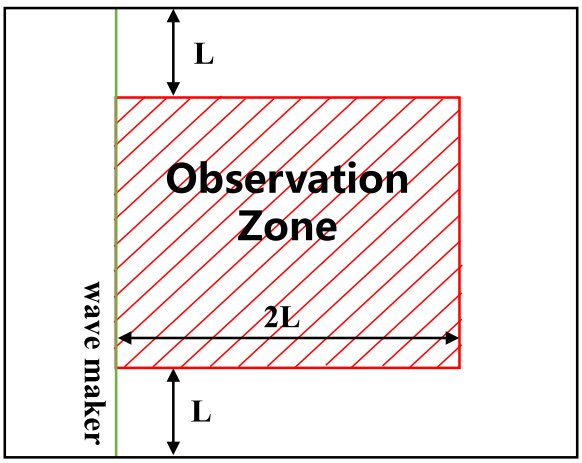

Fig. 21 Determination of the observation zone

oblique wave-current interactions, thus validating the feasibility of conducting non-collinear wave-current interaction simulations in a numerical basin.

(3) Noncollinear wave-current interactions differ from collinear interactions, and special attention should be given to disturbances from the sides of the wave basin to the observation zone during simulations. A stability analysis of the orthogonal wave-current interaction field was conducted to identify the effective observation zone for a numerical basin based on the orthogonal wave-current interactions. During the simulation, unstable regions are primarily concentrated near the sides and far from the wave mass source. When conducting numerical simulation studies on noncollinear wave-current interactions, the width of the basin should be increased as much as possible to minimize these effects.

Notably, there are still some shortcomings in the developed methods. The observation zone of the orthogonal wave-current interaction field not only involves wave elements and current velocity but also may be related to water depth, which should be considered in further research. In addition, the distance between wave height, still water level and center height of mass source is closely related, so the limitations of wave generation by mass source can be further explored in the future.

Acknowledgements
The authors would like to thank their colleagues from Southwest Jiaotong University and Zhejiang University for their assistance and discussions.

Authors' contributions
Conceptualization, KW and KH; Methodology, KW and KH; Investigation, KH; Supervision, KW; Writing—original draft, KW and KH; Writing—review and editing, KW and KH. All the authors have read and agreed to the published version of the manuscript.

Funding
This work was supported financially by the National Natural Science Foundation of China (Grant No. 52222804).

Availability of data and materials
The data will be made available upon request.

Declarations

Competing interests
The author(s) declare no potential conflicts of interest with respect to the research, authorship, and/or publication of this article.

Received: 28 February 2024 Accepted: 26 April 2024
Published online: 02 July 2024

References

Brevik I (1980) Flume experiment on waves and currents II. Smooth Bed Coastal Engineering 4:89–110
Brevik I, Bjorn A (1979) Flume experiment on wave and current. I Rippled Bed Coastal Engineering 3:149–177
Chen Y, Hsiao SC (2016) Generation of 3D water waves using mass source wavemaker applied to Navier-Stokes model. Coast Eng 109:76–95
Chen X, Chen Z, Xu G et al (2021) Review of wave forces on bridge decks with experimental and numerical methods. Adv Bridge Eng 2:1–24
Ding Y, Ma R, Li N (2015) A simulation model for three-dimensional coupled wave-current flumes. Engineering Mechanics 32(10):68–74+88.7
Guo J, Zhong C, Wang R et al (2022) Analysis of wind speed probability model of sea-crossing bridge affected by typhoons. Engineering Mechanics 39(S1):180–186
Jiang D, Tai W (1993) Joint refraction and diffraction model of random wave propagation in non-uniform flow field with gentle slope. Acta Oceanol Sin 15(06):37–46
Johnson JW (1947) The refraction of surface waves by currents. EOS Trans Am Geophys Union 28(6):867–874
Jonsson IG, Skougaard C, Wang JD (1970) Interaction between waves and currents. Coast Eng 1970:489–507
Kang A, Yin R, Zhu B et al (2020) Numerical simulation of wave-current force of cofferdam during construction of sea-crossing bridge based on LES. J Southwest Jiaotong University 55(3):537–544
Li Y (1984) Wave diffraction in a diagonal current. Port & Waterway Engineering 01:1–7
Li Y, Liu D, Chen B et al (2004) Wave diffraction in a diagonal current around the large-scale vertical circular cylinder. China Offshore Platform 03:1–9
Lim KY, Madsen OS (2016) An experimental study on near-orthogonal wave–current interaction over smooth and uniform fixed roughness beds. Coast Eng 116:258–274
Lin P, Liu F (1999) Internal wave-maker for Navier-Stokes equations models. J Waterw Port Coast Ocean Eng 125(4):207–215
Liu H, Wang B, Xue L et al (2013) Research progress on wave-current force of pile cap structure. Appl Math Mech 34(10):1098–1109
Longuet-Higgins MS, Stewart RW (1961) The changes in amplitude of short gravity waves on steady non-uniform currents. J Fluid Mech 10(4):529–549
Peregrine DH (1976) Interaction of water waves and currents. Adv Appl Mech 16:9–117
Qin S, Gao Z (2017) Developments and prospects of long-span high-speed railway bridge technologies in China. Engineering 3(6):787–794
Roache PJ (1997) Quantification of Uncertainty in Computational Fluid Dynamics. Annu Rev Fluid Mech 29:123–160
Samion SRL, Shaharuddin NH, Ali MSM (2019) Grid Convergence Study for Detached-Eddy Simulation of Flow over Rod-Airfoil Configuration Using OpenFOAM. IOP Conf Ser: Mater Sci Eng 491(1):12023

Thomas GP (1981) Wave-current interactions: an experimental and numerical study. Part 1. Linear waves. J Fluid Mech 110:457–474
Thomas GP (1990) Wave–current interactions: an experimental and numerical study. Part 2. Nonlinear waves. J Fluid Mech 216:505–536
Wang P, Zhao M, Du X (2019) Short-crested wave-current forces on composite bucket foundation for an offshore wind turbine. Math Probl Eng 2019. https://doi.org/10.6052/j.issn.1000-4750.2023.07.0525
Wei C, Zhou D, Ou J (2019) Wave and wave-current actions on a bridge tower: an experimental study. Adv Struct Eng 22(6):1467–1478
Wei K, Zhou C, Zhang M et al (2020) Review of the hydrodynamic challenges in the design of elevated pile cap foundations for sea-crossing bridges. Adv Bridge Eng 1(1):1–30
Wei K, Zhou C, Xu B (2022) Spatial distribution models of horizontal and vertical wave impact pressure on the elevated box structure. Appl Ocean Res 125:103245
Wei K, Shang D, Zhong X (2023b) Life-cycle thinking-based decision support framework for multispan simply supported bridges under typhoon-induced wave, current and surge conditions. Ocean Eng 288:115965
Wei K, Zhong X, Cai H et al (2024) Dynamic response of a sea-crossing cable-stayed suspension bridge under simultaneous wind and wave loadings induced by a landfall typhoon. Ocean Eng 293:116659
Wei K, Li H, Zhong X, et al. (2023) Study on extreme values and non-collinear characteristics of waves and current parameters in a sea strait under typhoons. Engineering Mechanics 1–11.
Whitehead JA (1998) Topographic control of oceanic flows in deep passages and straits. Rev Geophys 36(3):423–440
Whitham GB (1962) Mass, momentum and energy flux in water waves. J Fluid Mech 12(1):135–147
Xiao H, Huang W, Tao J et al (2013) Numerical modeling of wave-current forces acting on horizontal cylinder of marine structures by VOF method. Ocean Eng 67:58–67
Xie H, Liu X, Zhang Z et al (2021) Methodology of evaluating local dynamic response of a hull structure subjected to slamming loads in extreme sea. Ocean Eng 239:109763
Yakhot V, Orszag SA (1986) Renormalization group analysis of turbulence. I. Basic theory. J Sci Comput 1(1):3–51
Zhang X, Simons R, Zheng J et al (2022) A review of the state of research on wave-current interaction in nearshore areas. Ocean Eng 243:110202
Zhao M, Wang X, Wang P et al (2021) An accurate frequency-domain model of water interaction with cylinders of arbitrary shape during earthquakes. Adv Bridge Eng 2(1):1–17
Zhao R, Zheng K, Wei X et al (2022) State-of-the-art and annual progress of bridge engineering in 2021. Adv Bridge Eng 3(1):1–71

Publisher's Note